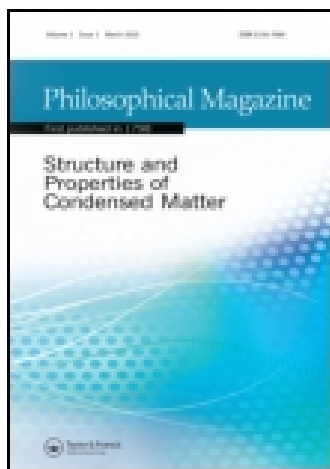


This article was downloaded by: [University of California, Los Angeles (UCLA)]

On: 02 April 2015, At: 15:57

Publisher: Taylor & Francis

Informa Ltd Registered in England and Wales Registered Number: 1072954 Registered office: Mortimer House, 37-41 Mortimer Street, London W1T 3JH, UK



Philosophical Magazine

Publication details, including instructions for authors and subscription information:

<http://www.tandfonline.com/loi/tphm20>

Orientation- and size-dependent room-temperature plasticity in ZrC crystals

S. Kiani^a, C. Ratsch^b, A.M. Minor^{cd}, S. Kodambaka^a & J.-M. Yang^a

^a Department of Materials Science and Engineering, University of California Los Angeles, Los Angeles, CA 90095, USA

^b Department of Mathematics and Institute for Pure and Applied Mathematics, University of California Los Angeles, Los Angeles, CA 90095, USA

^c Department of Materials Science and Engineering, University of California Berkeley, Berkeley, CA 94720, USA

^d Lawrence Berkeley National Laboratory, National Center for Electron Microscopy, Berkeley, CA 94720, USA

Published online: 16 Feb 2015.



[Click for updates](#)

To cite this article: S. Kiani, C. Ratsch, A.M. Minor, S. Kodambaka & J.-M. Yang (2015) Orientation- and size-dependent room-temperature plasticity in ZrC crystals, *Philosophical Magazine*, 95:9, 985-997, DOI: [10.1080/14786435.2015.1012568](https://doi.org/10.1080/14786435.2015.1012568)

To link to this article: <http://dx.doi.org/10.1080/14786435.2015.1012568>

PLEASE SCROLL DOWN FOR ARTICLE

Taylor & Francis makes every effort to ensure the accuracy of all the information (the "Content") contained in the publications on our platform. However, Taylor & Francis, our agents, and our licensors make no representations or warranties whatsoever as to the accuracy, completeness, or suitability for any purpose of the Content. Any opinions and views expressed in this publication are the opinions and views of the authors, and are not the views of or endorsed by Taylor & Francis. The accuracy of the Content should not be relied upon and should be independently verified with primary sources of information. Taylor and Francis shall not be liable for any losses, actions, claims, proceedings, demands, costs, expenses, damages, and other liabilities whatsoever or howsoever caused arising directly or indirectly in connection with, in relation to or arising out of the use of the Content.

This article may be used for research, teaching, and private study purposes. Any substantial or systematic reproduction, redistribution, reselling, loan, sub-licensing, systematic supply, or distribution in any form to anyone is expressly forbidden. Terms &

Conditions of access and use can be found at <http://www.tandfonline.com/page/terms-and-conditions>

Orientation- and size-dependent room-temperature plasticity in ZrC crystals

S. Kiani^a, C. Ratsch^b, A.M. Minor^{c,d}, S. Kodambaka^{a,*} and J.-M. Yang^{a,*}

^aDepartment of Materials Science and Engineering, University of California Los Angeles, Los Angeles, CA 90095, USA; ^bDepartment of Mathematics and Institute for Pure and Applied Mathematics, University of California Los Angeles, Los Angeles, CA 90095, USA; ^cDepartment of Materials Science and Engineering, University of California Berkeley, Berkeley, CA 94720, USA; ^dLawrence Berkeley National Laboratory, National Center for Electron Microscopy, Berkeley, CA 94720, USA

(Received 3 June 2014; accepted 22 January 2015)

Using *in situ* electron microscopy-based nanomechanical testing, we show that sub-micron-scale ZrC(100) and ZrC(111) single crystals exhibit size- and orientation-dependent room-temperature plasticity under compression. We identify $\{1\bar{1}0\}\langle 110\rangle$ and $\{001\}\langle 110\rangle$ as the active slip systems operating in ZrC(100) and ZrC(111) crystals, respectively. For both the orientations, yield strengths increase with decreasing crystal size. ZrC(111) is found to be up to $10\times$ softer than ZrC(100). Using density functional theory calculations, we attribute the observed anisotropy to surprisingly facile shear along $\{001\}\langle 110\rangle$ compared to $\{1\bar{1}0\}\langle 110\rangle$. Based upon our results, which provide important insights into plastic deformation modes operating in ZrC, we expect that slip systems other than $\{1\bar{1}0\}\langle 110\rangle$ can be softer and operate at low temperatures in NaCl-structured refractory transition-metal carbides and nitrides.

Keywords: carbides; plasticity; microscopy

1. Introduction

Advanced structural ceramics such as refractory transition-metal borides, carbides (TMCs), and nitrides (TMNs) [1–3], owing to a combination of strong ionic, covalent, and metallic bonds, exhibit superior thermomechanical properties, excellent wear, ablation, oxidation, and corrosion resistance, and are used as hard protective coatings and in aerospace structural components [4]. Among this class of materials, rocksalt (B1)-structured TMCs of group IV and V elements are hard (>20 GPa), stiff (Young's moduli >350 GPa), and high-melting ($T_m \gtrsim 3000$ K) solids with good electrical and thermal conductivities [5,6]. While TMCs subjected to indentation are known to slip at room-temperature [7,8] and ductile at elevated temperatures ($\gtrsim 0.3T_m$) [9–12], they are generally considered to be brittle under uniaxial loading or bending at low temperatures [10,13,14].

Room-temperature plasticity has been observed as early as the 1950s in B1-structured bulk ionic crystals [15], more recently, in single-crystals of SrTiO₃ [16] and, at smaller

*Corresponding authors. Email: kodambaka@ucla.edu (S. Kodambaka); jyang@seas.ucla.edu (J.-M. Yang)

length scales, in covalently bonded group IV and group III-V semiconductors [17–23]. However, there is no such data for B1-structured TMCs. Realization of similar plasticity in TMCs and other refractory ceramics would lead to greater improvements in life-time performance of these structural materials and could potentially open up new lower temperature applications. For B1-structured TMCs, indentation hardness is found to be highly anisotropic, and the operating slip systems varied with temperature and the transition-metal atoms [7,8]. Uniaxial compression of TiC(001) single-crystals revealed that $\{1\bar{1}0\}\langle 110\rangle$ is the most favourable slip system at temperatures below 600 °C, while $\{111\}\langle 1\bar{1}0\rangle$ was found to be active at higher temperatures [24,25]; in case of ZrC single-crystals, the critical-resolved shear stresses for slip along $\{110\}$ and $\{111\}$ were nearly the same over a range of temperatures between 1100 and 2000 °C. This behaviour is in distinct contrast with NaCl-structured ionic crystals such as MgO, which exhibit strongly anisotropic mechanical deformation behaviour [26]. While most existing studies focused on high-temperature deformation behaviour of TMCs, relatively little is known concerning the mechanisms leading to plasticity at low temperatures. Motivated by the existing literature on uniaxial compression of ZrC single-crystals at elevated temperatures [11], we chose ZrC as a model TMC and focused on understanding the room-temperature mechanical behaviour of single-crystals as a function of size and orientation.

In this study, we report *in situ* transmission electron microscopy (TEM) observations of size- and orientation-dependent plastic deformation of single-crystalline ZrC(100) and ZrC(111) pillars subjected to uniaxial compression at room-temperature. By simultaneously measuring structural changes and mechanical deformation occurring in the material in response to the applied load, we identify $\{1\bar{1}0\}\langle 110\rangle$ and $\{001\}\langle 110\rangle$ as the active slip systems in ZrC(100) and ZrC(111), respectively. We find that yield strength σ_y of the pillars increases with decreasing pillar diameter D . ZrC(111) pillars exhibit lower σ_y and a stronger size dependence than ZrC(100) pillars. These results are opposite to that observed in B1-structured ionic solids such as MgO and LiF [27,28]. Using density functional theory (DFT) calculations, we attribute the origin of this anisotropy to surprisingly easy shear along $\{001\}\langle 110\rangle$.

2. Experimental details

All of our *in situ* compression experiments are carried out using cylindrical ZrC pillars prepared via focused ion beam (FIB) milling of single-crystalline ZrC(100) and ZrC(111) wafers (2-mm-thick and 2-mm-diameter circular discs, from Applied Physics Technologies). First, the wafer is cut into two halves and one half of the crystal is mechanically polished to sub-100- μm thickness. Then the sample is mounted on a TEM stub and transferred to a FEI 235 FIB system. Pillars of diameters D between 0.1 and 0.55 μm with aspect ratios of 1.5–3.3, chosen to minimize buckling, are prepared using 30 kV Ga^+ beams in two steps. Initial coarse milling is carried out at an ion beam current of 20 nA followed by fine milling with 30 pA current. This milling procedure yielded pillars with a slightly tapered ($<3^\circ$) geometry.

In situ compression tests are carried out using a flat 3- μm -wide diamond punch using a Hysitron TEM PicoIndenter 95 in a JEOL 3010 TEM operated at 300 kV. Hysitron TEM PicoIndenter 95 employs a piezoelectric actuator for fine-scale positioning and a miniature transducer to measure applied load and displacement. Each of the ZrC(100) and ZrC(111) pillars is uniaxially compressed along $[100]$ and $[111]$, respectively, in

displacement-control mode at a constant loading rate of 10 nm/s. During each test, load-displacement data, video-rate (30 frames/s) TEM images, and selected area electron diffraction (SAED) patterns are acquired.

TEM image magnifications and acquisition times are varied to check for any electron beam-induced changes in our samples. We do not observe any such effects in our measurements. In order to determine slip systems, SAED patterns, along with bright- and dark-field TEM images of ZrC(111) and ZrC(100) pillars are obtained post-compression using a Titan 80–300 kV TEM after thinning and cleaning the pillars in a Fischione 1040 Nanomill. In the TEM, imaging conditions are chosen such that the contrast due to dislocations and slip traces are enhanced.

3. DFT calculations

In order to understand the origin of the anomalous orientation-dependent plasticity in ZrC, we used DFT and calculated uniaxial stresses required to deform stoichiometric ZrC single-crystals and energy barriers associated with slip and shear along the primary slip systems. All of our DFT calculations are performed with the FHI-AIMS code [29] using supercells with periodic boundary conditions and GGA-PBE for the exchange–correlation functional [30]. The slab consists of at least 12 layers that are periodic in the x and y directions and separated by at least 30 Å of vacuum along the z direction. We have carefully tested convergence of our results with respect to the slab and vacuum layer thicknesses, basis set, and the density of the (numerical) integration mesh. We have used parameters as they are implemented in FHI-AIMS in the default setting “light”. The results are essentially the same as those obtained with the default setting “tight”.

Ideal strengths of ZrC during uniaxial compression and tension as a function of crystal orientation are calculated following Ref. [31] as follows. The slab is incrementally strained in tension or in compression along the z direction and the total energy E_{tot} of the system is determined with DFT at each strain. (In these calculations, the lattice is not relaxed along x and y directions.) Normal tensile and compressive stresses are then calculated as $\sigma_{ij} = \frac{1}{V}(\partial E_{tot}/\partial \varepsilon_{ij})$, where V is the volume of the supercell and ε is the 3×3 strain tensor. We use both analytical as well as numerical evaluation of the stress as implemented in FHI-AIMS and get essentially the same results. The data presented here are obtained from the analytical evaluation.

Generalized stacking fault energy, defined as the energy per unit area required to shift one half of the supercell with respect to the other half, is calculated for each of the three planes (1 0 0), (1 1 0) and (1 1 1) along the three low-index directions $\langle 1 0 0 \rangle$, $\langle 1 1 0 \rangle$ and $\langle 1 1 1 \rangle$. In all the calculations, the top half of the slab is moved uniformly along the desired direction, until we reach a saddle point. All the atoms are constrained along the slip direction, but are fully relaxed in all other directions. The maximum energy change in these calculations is referred to as the unstable stacking fault energy, a measure of dislocation nucleation, and the results of these calculations are presented in the manuscript.

Ideal shear stresses and the total energies per unit volume required to induce shear strain are also calculated along the three primary slip systems. In these calculations, the entire slab is sheared. That is, we move the first layer a certain distance dx , until it reaches a saddle point. During shear, we then move the second layer by $2dx$, the third

layer by $3dx$, etc. This is in contrast to the above described stacking fault energy calculations, where the entire upper half of the slab is moved by dx .

4. *In situ* uniaxial compression test results

Figures 1(a)–(g) show representative TEM images, SAED pattern, and engineering stress σ vs. displacement data acquired *in situ* during compression of an $\sim 1\text{-}\mu\text{m}$ -long ZrC(100) pillar with $D = 0.30\ \mu\text{m}$. Figures 1(a)–(e) are bright-field TEM images extracted from a TEM video (see “ZrC(100)-Movie 1” in the Online Supplemental Data). In the images, the pillar is supported by the ZrC(100) substrate at the bottom and the diamond punch is in contact with the pillar at the top. Upon compression of the pillar, yielding occurred via slip. In this experiment, we observe localized deformation and the formation of shear bands near the top of the pillar that is in contact with the diamond punch. The first occurrence of shear, labelled 1 in Figure 1(b), at 60 nm is followed by the formation of a surface step (indicated by an arrow in Figure 1(c)) and formation of a second shear plane, labelled 2 in Figure 1(d) at ~ 80 nm. Figure 1(e) shows the post-compression morphology of the pillar. The observed phenomenon is characteristic of plastic deformation, typically observed in metals [32]. The localized deformation behaviour (see Figure 1(e)) is typical of all of our pillars and has also been observed in ionic crystals [27]. SAED pattern (Figure 1(f)) acquired from the compressed pillar indicates that the pillar retains its single-crystalline structure; that is, ZrC pillars do not undergo phase transformation and/or twinning due to compression.

Although *in situ* TEM movies suggest dislocation activity, we were unable to detect any dislocations in these pillars after the compression tests. We speculate that, due to the confined volume of the pillars, dislocations may have moved out of the pillars. From the analyses of SAED patterns and the shear traces observed in TEM images (see

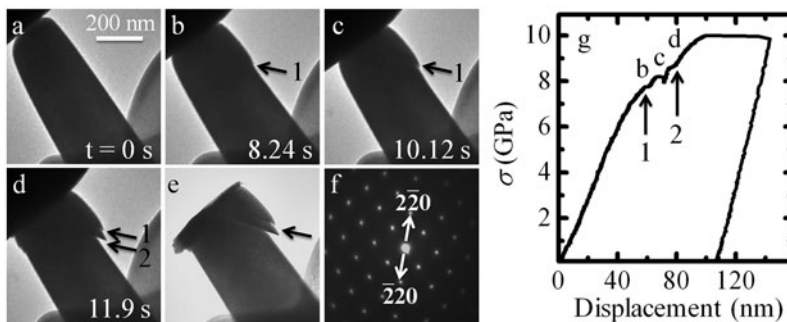


Figure 1. (a)–(d) Bright-field TEM images acquired *in situ* during displacement-controlled uniaxial compression of a ZrC(100) pillar with diameter $D = 0.30\ \mu\text{m}$. In this experiment, the pillar was loaded up to 100 nm. Arrows show the initiation and propagation of shear planes labelled 1 and 2 at ~ 60 and ~ 80 nm, respectively. (e) Bright-field TEM image of the pillar after the compression test. (f) Selected area electron diffraction (SAED) pattern acquired along $[001]$ zone axis from the pillar in Figure 1(e). The arrows in (e) and (f) highlight the $\{110\}$ slip planes. (g) Typical plot of engineering stress vs. displacement measured during compression of the pillar shown in Figures 1(a)–(e). Labels 1 and 2 correspond to displacement bursts resulting from shearing of the planes highlighted in Figures 1(c) and (d). (Extracted from “ZrC(100)-Movie 1”).

Figure 2 upper panel), we find that the normal to the shear plane traces passes through the $(2\bar{2}0)$ planes, indicating that the slip plane orientation is along $\{1\bar{1}0\}$. It is likely that $\langle 110 \rangle$, the direction with the shortest repeat distance in B1 lattice, is also the slip direction in our experiments. Based upon similar observations in all of the ZrC(100) pillars (see, for example, the lower panel in Figure 2), we suggest that the primary slip systems operating during uniaxial compression of ZrC(100) pillars are $\{1\bar{1}0\}\langle 110 \rangle$. This is plausible since the resolved shear stress during compression along $[100]$ is highest for the $\{1\bar{1}0\}\langle 110 \rangle$ slip systems and consistent with previous high-temperature uniaxial compression of ZrC(100) [11] and low-temperature indentation tests conducted on bulk group IV (100)-oriented TMCs [7,8].

The points 1 and 2 in the Figure 1(g) plot correspond to the times at which macroscopic shear events 1 and 2 occurred in the pillar (see Figures 1(b) and (d)). At smaller loads, displacement increases linearly with applied load, indicative of elastic deformation. At higher loads, we observe a non-linear increase in the displacement with increasing

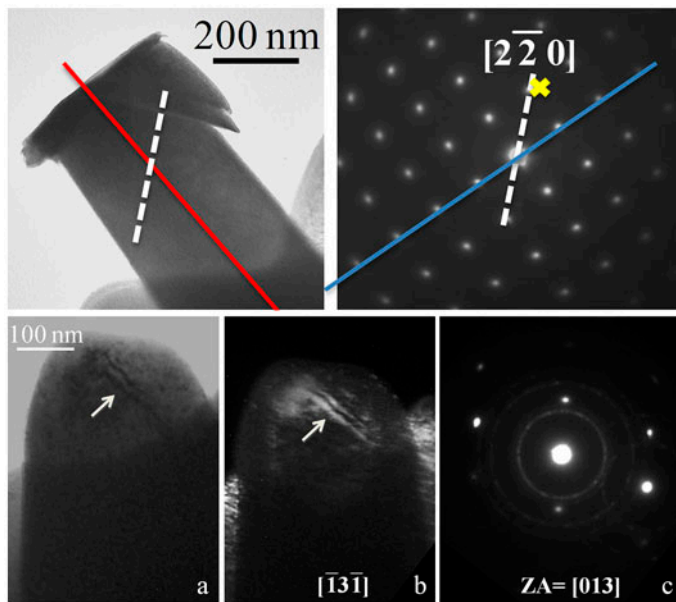


Figure 2. (colour online) (Upper panel) Bright-field TEM image and SAED pattern of the compressed ZrC(100) pillar shown in Figures 1(e) and (f), respectively. The solid red and dashed white lines in the TEM image are along the pillar axis $[100]$ and normal to the slip traces, respectively. The blue line passing through the central (000) spot in the SAED is drawn perpendicular to the red line and hence the diffraction spots lying on this line correspond to the $\{200\}$ planes. The white dashed line superposed on the SAED pattern is parallel to the line in TEM image and intersects, within the experimental uncertainties of $\sim 4^\circ$, the $(2\bar{2}0)$ spot highlighted by a yellow cross. Based upon these results, the slip plane orientation is identified as $\{1\bar{1}0\}$. (Lower panel) (a) Bright- and (b) dark-field TEM images obtained from a ZrC(100) pillar with $D = 0.28$ μm after shear deformation. The dark-field image in (b) is obtained using $[\bar{1}31]$ reflection. Slip traces (highlighted by the arrows) indicate that the slip plane orientation is $\{110\}$ determined following the approach presented in the upper panel. (c) SAED pattern of the pillar along $[013]$ zone axis, indicating that the pillar retains its single-crystalline structure post-compression.

stress as the pillar begins to deform plastically. In this experiment, the deviation from linearity in the stress-displacement data occurred at an engineering stress of ~ 6.7 GPa. This value, corresponding to the point of transition from elastic to plastic deformation, is the yield strength, σ_y . As we show later, σ_y increases with decreasing size D . All of these results are representative of 9 different ZrC(100) pillars prepared and tested using similar procedure.

In contrast to ZrC(100), ZrC(111) pillars do not exhibit shear bands. Figures 3(a)–(d) are representative bright-field TEM images extracted from a video (see “ZrC(111)-Movie 2-Part II”) recorded during the compression of ~ 0.55 - μm -long ZrC(111) pillar with $D = 0.18$ μm . We note that the TEM images show contrast near the tip of the pillar, some of which was also observed in the as-prepared sample acquired prior to loading (please see Online Supplemental Data). In this particular experiment, the sample was first uniaxially compressed up to a displacement of 50 nm after which the applied load was removed. The same sample was then loaded up to 100 nm, and this portion of the data is shown in Figure 3. The complete set of data and the corresponding movies (“ZrC(111)-Movie 2-Part I” and “ZrC(111)-Movie 2-Part II”) are presented in the Online Supplemental Data. While there are some noticeable changes to the microstructure of the sample due to initial loading, we do not have sufficient data to relate these changes to the mechanical behaviour of the sample at this time. *In situ* TEM videos reveal nucleation, motion, and tangling of dislocations within the pillars. Here, we do not observe any slip traces. Figure 3(e) is a post-compression image of the same pillar, which shows that its length decreased by ~ 60 nm while the diameter increased by ~ 20 nm. The SAED pattern in Figure 3(f), acquired from the ZrC(111) pillar after the test, indicates that neither the crystal structure nor the crystallinity of the pillar are affected by the compression. Figure 3(g) is a plot of σ vs. displacement data acquired during compression of the pillar. The smooth, non-linear variation in displacement with applied load and the absence of any abrupt changes (“pop-ins”), associated with slip, are consistent with

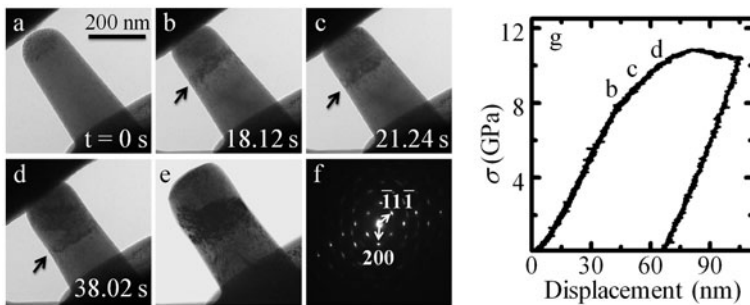


Figure 3. (a)–(d) Bright-field TEM images extracted from a video recorded during uniaxial compression of a 0.18- μm -diameter ZrC(111) pillar up to 100 nm. This particular sample was first loaded up to 50 nm and unloaded prior to acquiring the data shown here. For complete set of data, please see Online Supplemental Data and the movie “ZrC(111)-Movie 2-Part I”. The contrast changes visible in the images, highlighted by the arrows, are due to the nucleation and motion of dislocations. (e) Post-compression TEM image of the pillar. (f) SAED pattern of the compressed pillar in Figure 2(e) along $[0\ 1\ 1]$ zone axis. (g) Associated plot of σ vs. displacement data for the pillar. (Extracted from “ZrC(111)-Movie 2-Part II”).

plastic deformation via dislocation motion. This behaviour is typical of all the 9 different ZrC(111) pillars that we have tested. Since the resolved shear stress on $\{1\bar{1}0\}\langle 110\rangle$ slip systems is zero during loading along $[111]$, the observed plastic deformation must be due to the operation of other slip systems such as $\{001\}\langle 110\rangle$ and/or $\{1\bar{1}1\}\langle 110\rangle$, with Schmid factors of 0.47 and 0.27, respectively.

Analysis of TEM images shown in Figures 4(a)–(c) indicates that $\{001\}\langle 110\rangle$ slip systems are active during compression of the ZrC(111) pillars. For ZrC(111) pillars, based on **g**·**b** invisibility criterion and imaging using two known reflections $[1\bar{1}1]$ and $[\bar{1}\bar{1}1]$, we determine the slip direction as $[101]$. From the images of slip traces, we identify one of the slip planes as (010) . That is, the family of slip systems $\{001\}\langle 110\rangle$ is operative in ZrC(111) pillars. While the activation of $\{001\}\langle 110\rangle$ slip systems at room-temperature during uniaxial compression of TMCs or other NaCl-structured compounds has never been reported, slip along $\{001\}\langle 110\rangle$ has been observed at higher temperatures during the compression of MgO(111) [26] and ZrC(111) crystals [11]. Interestingly, the critical stresses required to uniaxially compress ZrC(111) crystals were found to be higher than those required for the compression of ZrC(001) or ZrC(110) crystals [11].

Our *in situ* observations (see Movies 1 and 2) provide direct evidence for plastic deformation of ZrC crystals under uniaxial loading at room-temperature, generally not expected in refractory TMCs. The observed behaviour in ZrC, which is commonly considered to be brittle, can be attributed to the small sizes of the crystals. Studies have shown that the compressive stress required to fracture increases with decreasing size of a brittle material and that there exists a threshold size below which yielding, rather than brittle fracture, is favored [22,33,34]. Moreover, the pillars are single-crystals, which at sub-micron-scale compared to bulk are likely to have a lower density of surface and bulk defects that could act as stress risers and induce fracture. Hence, the pillars can withstand higher stresses that enable nucleation and motion of dislocations leading to the observed plastic deformation. While FIB milling can introduce structural defects and hence affect the mechanical behaviour of the pillars, we argue, based upon the size-dependent yielding discussed below, that FIB milling has little effect on the observed plasticity in ZrC pillars.

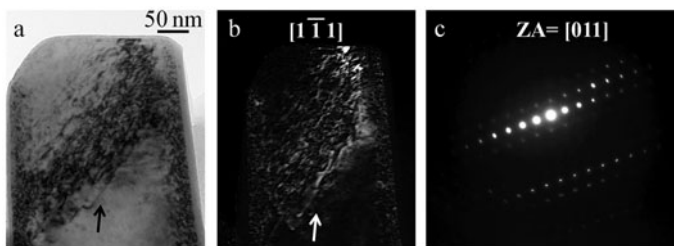


Figure 4. (a) Bright- and (b) dark-field TEM images of a ZrC(111) pillar with $D = 0.26 \mu\text{m}$ acquired after the compression test. The dark-field image is obtained using $[1\bar{1}1]$ reflection. Arrows highlight the dislocation lines. The darker contrast bands visible in Figure 4(a) are oriented along $\sim 55^\circ$ with respect to $[111]$ and are due to dislocations in $\{001\}$. (c) SAED pattern of the pillar along $[011]$ zone axis. We find that the pillar retains single-crystallinity after compression.

To gain better insights into the plastic deformation behaviour in ZrC, we now focus on the effect of ZrC crystal size on the mechanical behaviour. Figures 5(a) and (b) show typical plots of engineering stress vs. strain measured during uniaxial compression of ZrC(100) and ZrC(111) pillars, respectively, of different D . This data is a subset of the measurements collected from 9 ZrC(100) and 9 ZrC(111) pillars of D between 0.10 and 0.55 μm . For a given crystallographic orientation, all the pillars exhibit similar deformation behaviour. And, for both orientations, the maximum stresses withstood by the pillars before failure increase with decreasing D (see Figure 5).

Yield points and hence σ_y values are extracted from such stress-displacement curves as follows. First, a fraction of the stress-displacement data corresponding to the transition from elastic to plastic deformation is plotted on log-log scale as shown in Figure 6(a). In such log-log plots, the elastic and plastic portions of the stress-displacement data can be fit with straight lines of different slopes. The point of intersection of these two lines is identified as the yield point and the corresponding stress value is σ_y . Figure 6(a) shows a typical log-log plot along with least-squares fits to the data. Using a similar procedure, we determined σ_y for all the 18 ZrC pillars. Figure 6(b) is a plot of σ_y vs. D , which shows that σ_y varies between ~ 0.5 and 9 GPa. We note that the accuracy of the σ_y values extracted from our tests depends on the pillar-punch geometry. While the measurement uncertainties associated with pillar-punch misalignment are not known, based upon the compression tests carried out on 6 sets of pillars of similar sizes, we find that the maximum variation in σ_y is $\simeq 1$ GPa. For ZrC, the only available σ_y data are obtained from uniaxial compression of bulk ZrC single-crystals at high- T , which indicates that σ_y decreases from ~ 100 s of MPa at $T \simeq 1100$ $^{\circ}\text{C}$ to ~ 10 s of MPa at $T \simeq 2000$ $^{\circ}\text{C}$ [11]. We cannot directly extrapolate this high- T data to compare with our room- T results, since the loading rates are $\sim 10\times$ higher than those used in our experiments and crystal composition may be different from that of our samples. However, the σ_y values (1–10 GPa) obtained in our experiments are plausible and within the range of the ideal yield strength, which is expected to be a fraction (1/10 or 1/20) of the Young's modulus [35] and 1/3 of the hardness [36].

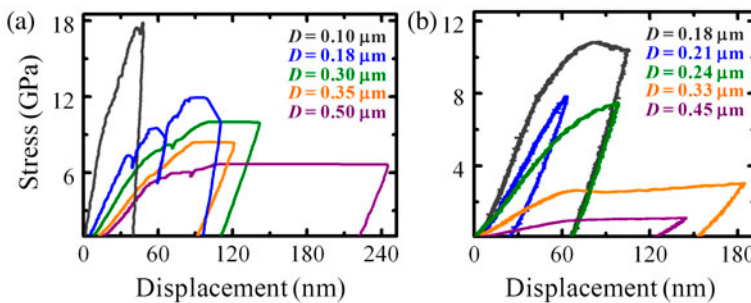


Figure 5. (colour online) Plots of engineering stress vs. strain for (a) ZrC(100) and (b) ZrC(111) pillars with D between 0.10 and 0.50 μm . All the data are acquired during compression of the pillars in displacement-controlled mode up to 100 nm of displacement and hence the maximum strains in the plots do not correspond to fracture.

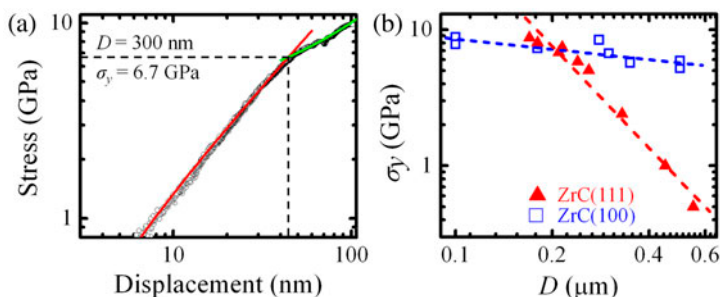


Figure 6. (colour online) (a) Log–log plot of a portion of the engineering stress vs. displacement data presented in Figure 1(g). For clarity, only the data around the transition from elastic to plastic deformation are shown. The red and green lines are least-squares fits to the data using which the yield point and yield strength σ_y are determined. (b) Log–log plot of σ_y vs. D for all the ZrC(111) (\blacktriangle) and ZrC(100) (\square) pillars. The dashed lines are linear least-squares fits to the (100) and (111) data, which serve as guides to the eye.

The data in Figure 6(b) indicate that yield strengths $\sigma_{y,100}$ and $\sigma_{y,111}$ of both ZrC(100) and ZrC(111) pillars increase with decreasing D . Similar size-dependences in $\sigma_y(D)$ have been observed in metal, covalent, and ionic crystals [27,32,37,38] and are attributed to (1) dislocation starvation [39,40], a process where defect density decreases with the crystal size, (2) dislocation truncation in small samples leading to increased flow stress [41,42], and to (3) enhanced dislocation nucleation, mobility, shielding, and limited dislocation multiplication rates at small length scales [37,38,43,44]. While we cannot determine which of these mechanisms control the observed size-dependent yielding, the differences between the size-effects observed in ZrC(100) and ZrC(111) pillars offer some insight into their mechanical responses. We find that $\sigma_{y,111}(D)$ varies steeply from ~ 0.5 GPa to ~ 9 GPa with D . In comparison, $\sigma_{y,100}(D)$ changes from ~ 5 GPa to ~ 9 GPa with D and $\sigma_{y,111}(D) < \sigma_{y,100}(D)$ for all $D \gtrsim 0.20 \mu\text{m}$. This finding is consistent with the expectation that the effect of size on σ_y is more (less) pronounced in crystals with smaller (higher) shear stress [27]. Both these results are opposite to what has been reported for similar-structured ionic crystals such as LiF and MgO, where $\sigma_{y,100}$ exhibits stronger size-dependence than $\sigma_{y,111}$ and $\sigma_{y,100}(D) < \sigma_{y,111}(D)$ [27,28]. Furthermore, both strain-hardening exponents $\{n\}$ and coefficients K , measures of dislocation multiplicity and interactions, appear to scale with D for ZrC(111) but vary little for ZrC(100) pillars as shown in Figure 7. To this purpose, true stress (σ_T) and true strain (ε_T) values are first calculated from the stress-displacement data in the range between the yield point and up to 20% engineering strain. Both n and K are then extracted by fitting σ_T vs. ε_T data with the equation of the form $\sigma_T = K\varepsilon_T^n$. Based upon these results, we suggest that the mechanical response of ZrC(111) is more sensitive than ZrC(100) to defects (e.g. anion vacancies and dislocations). The observation of yielding in ZrC(111) at significantly low stresses compared to ZrC(100) ($\sigma_{y,111} \sim \sigma_{y,100}/10$ at $D > 0.5 \mu\text{m}$) is unexpected since $\{1\bar{1}0\}\langle 110\rangle$ slip systems are generally believed to be the softer slip systems operating in group IV TMCs and TMNs [1]. While crystal stoichiometry could influence the absolute values of σ_y [6,8,14], we show below that defect-free ZrC(111) is expected to be softer than ZrC(100) under compression.

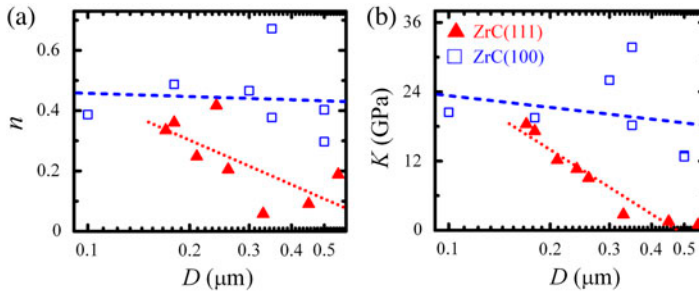


Figure 7. (colour online) Semi-log plots of (a) Strain-hardening exponent n and (b) strain-hardening coefficient K as a function of D for ZrC(111) (\blacktriangle) and ZrC(100) (\square) pillars. The dotted and dashed lines are guides to the eye. While there is considerable scatter in the data, values of both n and K are smaller and vary markedly with D for ZrC(111) compared to ZrC(100) pillars.

5. DFT calculation results

Figures 8(a) and (b) are representative stress–strain plots obtained by applying compressive and tensile stresses, respectively, on ZrC(100) and ZrC(111) crystals. Figure 8(a) shows stress σ vs. strain ε data calculated for uniaxial compression of ZrC(100) and ZrC(111) crystals. We find that uniaxial compression of ZrC along $[1\bar{1}1]$ is easier compared to compression along $[100]$. For example, ideal stress required to compress ZrC(111) by 10% is ~ 19 GPa. In comparison, ~ 80 GPa is required to compress ZrC(100) by the same amount. That is, ZrC(111) is softer under uniaxial compression than ZrC(100). (In contrast, ZrC(100) deforms easily under tension compared to ZrC(111) as shown in Figure 8(b).) Although all our calculations are carried out using perfect, dislocation-free crystals and the theoretical stresses are over $10\times$ higher than the measured values, the DFT results are in qualitative agreement with the experimental data. Calculated unstable stacking fault energies, measure of resistance to dislocation nucleation [45], are found to be lowest ($0.141\text{ eV}/\text{\AA}^2$) along $\{1\bar{1}0\}\langle 110\rangle$ followed by $\{1\bar{1}1\}\langle 110\rangle$ ($0.156\text{ eV}/\text{\AA}^2$) and $\{001\}\langle 110\rangle$ ($0.164\text{ eV}/\text{\AA}^2$). That is, $\{1\bar{1}0\}\langle 110\rangle$ is energetically the most favourable slip system for dislocation nucleation in ZrC. However, the total energy per unit volume required to shear, a measure of ideal shear stress,

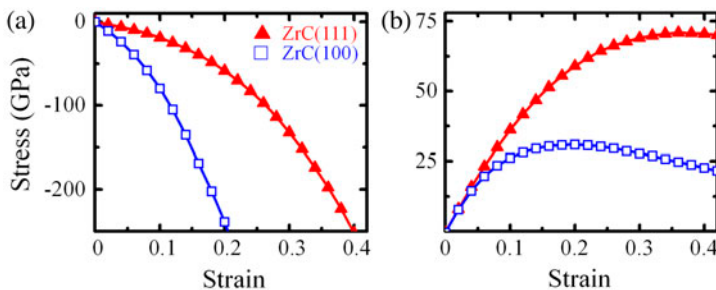


Figure 8. (colour online) Calculated uniaxial (a) compressive and (b) tensile stresses plotted as a function of lattice strain ε in ZrC(111) (\blacktriangle) and ZrC(100) (\square) crystals.

is found to be lowest ($0.077 \text{ eV}/\text{\AA}^3$) for $\{001\}\langle 110 \rangle$ compared to $0.331 \text{ eV}/\text{\AA}^3$ for $\{1\bar{1}0\}\langle 110 \rangle$ and $0.305 \text{ eV}/\text{\AA}^3$ for $\{1\bar{1}1\}\langle 110 \rangle$. That is, $\{001\}\langle 110 \rangle$ and $\{1\bar{1}0\}\langle 110 \rangle$ are the soft and hard slip systems in ZrC, respectively, consistent with our experimental results.

6. Discussion

The observed orientation-dependence in ZrC with easy slip along $\{100\}\langle 110 \rangle$, the close-packed slip system in B1-structured compounds, is qualitatively comparable to the operation of $\{111\}\langle 110 \rangle$ and $\{110\}\langle 111 \rangle$, the close-packed slip systems in face-centred and body-centred cubic metals, respectively. That is, the mechanical response of ZrC subjected to compressive stresses is similar to that of a cubic metal rather than a B1-structured ionic compound, such as MgO and LiF. This is probably expected since the electronic structures of B1-structured ZrC and other TMCs and TMNs are expected to be different from that of ionically-bonded MgO or LiF [6,14]. Even among the selected number of B1-structured Group IV and V TMCs, the nature and relative strengths of metal-metal and metal-carbon (or nitrogen in case of TMNs) bonds, vary with the valence electron concentration in the lattice [46], covalent radii of the metal cations, and crystal orientation. As a result, plastic deformation pathways [1] and overall ductility and hardness of these compounds [47] vary within the same Group (e.g. from TiC vs. ZrC) and from Group IV to Group V (e.g. TiC vs. VC) [8,48–50]. While DFT offers some insights into the mechanical response of ideal, defect-free, ZrC crystals, the calculations are limited to small cell sizes. To fully understand the electronic origins of plastic deformation in this class of materials, molecular dynamics simulations and multi-scale modelling of dislocation dynamics and the effect of vacancies are necessary. This, however, is a computationally challenging task and beyond the scope of this study.

The observed phenomenon of room-temperature plasticity is not specific to ZrC, but should also be expected in single-crystals of other NaCl-structured TMCs and TMNs. Based upon the fact that multiple slip systems are active at room-temperature, we suggest that carefully prepared polycrystalline TMC samples will also undergo plastic deformation at low temperatures. Since the loading rate, which in our experiments is 10 nm/s, and crystal size could influence the observed phenomena, additional mechanical tests conducted at different loading rates and using larger crystals are necessary to better understand the ductile deformation characteristics in this class of materials.

7. Summary

In summary, we investigated the room-temperature mechanical behaviour of ZrC(100) and ZrC(111) crystals using a combination of *in situ* electron microscopy-based mechanical testing and DFT calculations. We find that ZrC crystals undergo plastic deformation and exhibit size-dependent yield strengths, indicating that dislocations are mobile in this class of compounds. The measurements of yield strengths as a function of crystal orientation reveal that at least two slip systems ($\{1\bar{1}0\}\langle 110 \rangle$ and $\{001\}\langle 110 \rangle$) are active at room-temperature. DFT calculations support our finding that deformation along $\{001\}\langle 110 \rangle$ is easier than along the commonly expected $\{1\bar{1}0\}\langle 110 \rangle$ slip systems in B1-structured compounds. We suggest that DFT calculations of unstable stacking fault

energies alone may not be sufficient to correctly identify the preferred slip systems in ZrC and probably other transition-metal carbides. Additional calculations, such as energies associated with shear and experimental investigation of the effect of sample microstructure (e.g. dislocation density) can help provide better insights into the deformation behaviours into this class of materials. We expect that other transition-metal carbides and nitrides will also exhibit plasticity at low-temperatures. Insights gained from these studies could open up the possibility of designing hard-yet-ductile ceramic nanocomposites, free-standing thin films, and nanostructures for new micro- and nanomechanical applications.

Funding

SK and JMY are thankful for the funding from the Air Force Office of Scientific Research (Dr Ali Sayir) [grant number FA9550-10-1-0496]. CR gratefully acknowledges support from National Science Foundation [grant number DMS-0931852]. The *in situ* electron microscopy experiments are conducted as part of a user project at the National Center for Electron Microscopy, Lawrence Berkeley National Laboratory, supported by the Office of Science, Office of Basic Energy Sciences, of the US Department of Energy [grant number DE-AC02-05CH11231].

Supplemental data

Supplemental data for this article can be accessed here <http://dx.doi.org/10.1080/14786435.2015.1012568>.

References

- [1] L.E. Toth, *Transition metal carbides and nitrides*. Vol. 7, Academic Press, New York, 1971.
- [2] D.B. Marshall and J. Ritter, *Am. Ceram. Soc. Bull. (United States)* 66 (1987) p.309.
- [3] R. Raj, *J. Am. Ceram. Soc.* 76 (2005) p.2147.
- [4] W.G. Fahrenholtz, G.E. Hilmas, I.G. Talmy and J.A. Zaykoski, *J. Am. Ceram. Soc.* 90 (2007) p.1347.
- [5] W.S. Williams, *Science* 152 (1966) p.34.
- [6] G.E. Hollox, *Mater. Sci. Eng.* 3 (1968) p.121.
- [7] D.J. Rowcliffe and G.E. Hollox, *J. Mater. Sci.* 6 (1971) p.1270.
- [8] R. Hannink, D. Kohlstedt and M. Murray, *Proc. Royal Soc. A: Math. Phys. Eng. Sci.* 326 (1972) p.409.
- [9] W.S. Williams, *J. Appl. Phys.* 35 (1964) p.1329.
- [10] A. Kelly and D. Rowcliffe, *J. Am. Ceram. Soc.* 50 (1967) p.253.
- [11] D.W. Lee and J.S. Haggerty, *J. Am. Ceram. Soc.* 52 (1969) p.641.
- [12] N. De Leon, B. Wang, C.R. Weinberger, L.E. Matson and G.B. Thompson, *Acta Mater.* 61 (2013) p.3905.
- [13] W.S. Williams and R.D. Schaal, *J. Appl. Phys.* 33 (1962) p.955.
- [14] W.S. Williams, *Prog. Solid State Chem.* 6 (1971) p.57.
- [15] A. Gorum, E. Parker and J. Pask, *J. Am. Ceram. Soc.* 41 (1958) p.161.
- [16] P. Gumbsch, S. Taeri-Baghadrani, D. Brunner, W. Sigle and M. Rühle, *Phys. Rev. Lett.* 87 (2001) p.085505.
- [17] A. Minor, E. Lilleodden, M. Jin, E. Stach, D. Chrzan and J. Morris, *Philos. Mag.* 85 (2005) p.323.
- [18] D. Ge, A. Minor, E. Stach and J. Morris Jr, *Philos. Mag.* 86 (2006) p.4069.

- [19] J. Deneen, W. Mook, A. Minor, W. Gerberich and C.B. Carter, *J. Mater. Sci.* 41 (2006) p.4477.
- [20] X.D. Han, Y.F. Zhang, K. Zheng, X.N. Zhang, Z. Zhang, Y. Hao, X. Guo, J. Yuan and Z. Wang, *Nano Lett.* 7 (2007) p.452.
- [21] F. Östlund, K. Rzepiejewska-Malyska, K. Leifer, L.M. Hale, Y. Tang, R. Ballarini, W.W. Gerberich and J. Michler, *Adv. Funct. Mater.* 19 (2009) p.2439.
- [22] F. Östlund, P.R. Howie, R. Ghisleni, S. Korte, K. Leifer, W.J. Clegg and J. Michler, *Philos. Mag.* 91 (2011) p.1190.
- [23] S.R. Jian, T.H. Sung, J. Huang and J.Y. Juang, *Appl. Phys. Lett.* 101 (2012) p.151905.
- [24] D. Chatterjee, M. Mendiratta and H. Lipsitt, *J. Mater. Sci.* 14 (1979) p.2151.
- [25] G.E. Hollox and R.E. Smallman, *J. Appl. Phys.* 37 (1966) p.818.
- [26] C.O. Hulse, S.M. Copley and J.A. Pask, *J. Am. Ceram. Soc.* 46 (1963) p.317.
- [27] S. Korte and W. Clegg, *Philos. Mag.* 91 (2011) p.1150.
- [28] R. Soler, J.M. Molina-Aldareguia, J. Segurado, J. Llorca, R.I. Merino and V.M. Orera, *Int. J. Plast.* 36 (2012) p.50.
- [29] V. Havu, V. Blum, P. Havu and M. Scheffler, *J. Comput. Phys.* 228 (2009) p.8367.
- [30] J.P. Perdew, K. Burke and M. Ernzerhof, *Phys. Rev. Lett.* 77 (1996) p.3865.
- [31] O.H. Nielsen and R.M. Martin, *Phys. Rev. Lett.* 50 (1983) p.697.
- [32] M.D. Uchic, P.A. Shade and D.M. Dimiduk, *Ann. Rev. Mater. Res.* 39 (2009) p.361.
- [33] K. Kendall, *Nature* 272 (1978) p.710.
- [34] K. Kendall, *Proc. Royal Soc. A: Math. Phys. Eng. Sci.* 361 (1978) p.245.
- [35] D.L. Price, B.R. Cooper and J.M. Wills, *Phys. Rev. B* 46 (1992) p.11368.
- [36] S.H. Jhi, S.G. Louie, M.L. Cohen and J. Morris Jr, *Phys. Rev. Lett.* 87 (2001) p.75503.
- [37] E.M. Nadgorny, D.M. Dimiduk and M.D. Uchic, *Size effects in LiF micron-scale single crystals of low dislocation density*, in *Proceedings of the Materials Research Society Symposium*, Cambridge University Press, 2007, p.55.
- [38] W. Gerberich, J. Michler, W. Mook, R. Ghisleni, F. Östlund, D. Stauffer and R. Ballarini, *J. Mater. Res.* 24 (2009) p.898.
- [39] Z.W. Shan, R.K. Mishra, S.A.S. Asif, O.L. Warren and A.M. Minor, *Nat. Mater.* 7 (2008) p.115.
- [40] J.R. Greer, J.Y. Kim and M.J. Burek, *J. Minerals, Metals Mater. Soc.* 61 (2009) p.19.
- [41] T.A. Parthasarathy, S.I. Rao, D.M. Dimiduk, M.D. Uchic and D.R. Trinkle, *Scr. Mater.* 56 (2007) p.313.
- [42] D. Kiener and A.M. Minor, *Nano Lett.* 11 (2011) p.3816.
- [43] S.I. Rao, D.M. Dimiduk, T.A. Parthasarathy, M.D. Uchic, M. Tang and C. Woodward, *Acta Mater.* 56 (2008) p.3245.
- [44] F. Östlund, K. Rzepiejewska-Malyska, K. Leifer, L.M. Hale, Y. Tang, R. Ballarini, W.W. Gerberich and J. Michler, *Adv. Funct. Mater.* 19 (2009) p.2439.
- [45] J.R. Rice, *J. Mech. Phys. Solids* 40 (1992) p.239.
- [46] S.H. Jhi, J. Ihm, S.G. Louie and M.L. Cohen, *Nature* 399 (1999) p.132.
- [47] D.G. Sangiovanni, V. Chirita and L. Hultman, *Phys. Rev. B* 81 (2010) p.104107.
- [48] H. Kindlund, D.G. Sangiovanni, L. Martinez-de-Olcoz, J. Lu, J. Jensen, J. Birch, I. Petrov, J.E. Greene, V. Chirita and L. Hultman, *APL Mat.* 1 (2013) p.042104.
- [49] H. Kindlund, D.G. Sangiovanni, J. Lu, J. Jensen, V. Chirita, J. Birch, I. Petrov, J.E. Greene and L. Hultman, *Acta Mater.* 77 (2014) p.394.
- [50] H. Kindlund, D.G. Sangiovanni, J. Lu, J. Jensen, V. Chirita, I. Petrov, J.E. Greene and L. Hultman, *J. of Vac. Sci. & Technol., A* 32 (2014) p.030603.